

Detection of New Galaxy Candidates at $z > 11$ in the JADES Field Using JWST NIRCcam

Priyanka Chakraborty^{1,2} *, Arnab Sarkar^{2,3} , Scott Wolk¹ , Benjamin Schneider³ , Nancy Brickhouse¹ , Kenneth Lanzetta⁴, Adam Foster¹ , Randall Smith¹ 

¹Center for Astrophysics | Harvard & Smithsonian, Cambridge, MA 02138, USA

²Department of Physics, University of Arkansas, 825 West Dickson Street, Fayetteville, AR 72701, USA

³Kavli Institute for Astrophysics and Space Research, Massachusetts Institute of Technology, 70 Vassar St, Cambridge, MA 02139

⁴Stony Brook University, Stony Brook, NY 11794-3800

Accepted XXX. Received YYY; in original form ZZZ

ABSTRACT

We report the detection of six new galaxy candidates with photometric redshifts $z > 11$ within the JWST Advanced Deep Extragalactic Survey (JADES) GOODS-S and GOODS-N fields. These new candidates are detected through meticulous analysis of NIRCcam photometry in eight filters spanning a wavelength range of 0.8–5.0 μm . Photometric redshifts of these galaxy candidates are independently measured utilizing spectral energy distribution (SED) fitting techniques using EAZY and BAGPIPES codes, followed by visual scrutiny. One of these galaxy candidates is located in GOODS-S field, while the remaining five galaxies are located in GOODS-N field. Our analysis reveals that the stellar masses of these galaxies typically range from $\log M_*/M_\odot = 7.75\text{--}8.75$. Furthermore, these galaxies are typically young with their mass-weighted ages spanning from 80 to 240 Myr. Their specific star formation rates (sSFR), quantified as $\log(\text{sSFR}/\text{Gyr})$, are measured to vary between ~ 0.95 to 1.46. These new galaxy candidates offer a robust sample for probing the physical properties of galaxies within the first few hundred Myr of the history of the Universe. We also analyze the relationship between star formation rate (SFR) and stellar mass (M_*) within our sample. Continued investigation through spectroscopic analysis using JWST/NIRSpec is needed to spectroscopically confirm these high-redshift galaxy candidates and investigate further into their physical properties. We plan to follow up on these candidates with future NIRSpec observations.

Key words: galaxies: high-redshift, galaxies: photometry, galaxies: distances and redshifts, infrared: galaxies

1 INTRODUCTION

The galaxies that emerged within the first few hundred million years after recombination are believed to have played a crucial role in shaping the early Universe by hosting its first stars. This first generation of stars initiated the process of ionizing neutral hydrogen throughout the cosmos. While reionization is generally understood to have occurred within the first billion years following the Big Bang, the precise mechanisms and the specific types of galaxies responsible for this phenomenon remain largely elusive and subject to ongoing debate (e.g., Barkana & Loeb 2001; Bromm & Larson 2004; Fan et al. 2006; Bromm & Yoshida 2011; Stark 2016; Ouchi et al. 2020). Thus, studying early galaxies is crucial for understanding their formation and evolution over billions of years, revealing insights into the physical processes that shaped them and their role in re-ionizing the Universe.

Over the past decade, deep surveys conducted by the Hubble Space Telescope (HST) discovered thousands of galaxies, significantly improving our understanding of the properties and demographics of

galaxies up to $z \sim 11$ (Ellis et al. 2013; Ishigaki et al. 2015; Finkelstein et al. 2015; McLeod et al. 2016; Bhatwadekar et al. 2019; Bouwens et al. 2021). These surveys included the Hubble Ultra-Deep Field (HUDF, Beckwith et al. 2006), HUDF09 (Bouwens et al. 2011), HUDF12 (Ellis et al. 2013), the HST Great Observatories Origins Deep Survey (GOODS, Giavalisco et al. 2004), and many others (e.g., Scoville et al. 2007; Coe et al. 2019). However, the limited near-infrared (NIR) coverage of the HST, along with its moderate light-collecting capacity, limited the exploration of the evolution of galaxies at earlier ($z > 11$) epochs.

The method for selecting high-redshift galaxies has primarily been driven by photometry (Schenker et al. 2013; Bouwens et al. 2015). This technique exploits the absorption of ultraviolet light by neutral hydrogen within, around, and between distant galaxies. This absorption produces a distinctive spectral feature known as the “Lyman- α break,” observable at 912 Å in the spectral energy distribution (SED) of the galaxy (Sarkar & Samui 2019). The redshifts of these galaxies are determined by fitting their observed SEDs to either simulated or observed galaxy SEDs with known physical properties. This method incorporates more data than pure color selection alone (Bolzonella et al. 2000). To effectively apply this approach, accurate template

* E-mail: priyanka.chakraborty@cfa.harvard.edu

SEDs covering the entire color space of photometry are necessary, accounting for factors such as dust extinction and intergalactic medium (IGM) absorption. However, this procedure becomes less certain for high-redshift galaxies due to the scarcity of ultraviolet (UV) and optical SEDs for early galaxies (e.g., Stark 2016).

The commissioning of the James Webb Space Telescope (JWST) (Rigby et al. 2023) has opened a new window into the discovery and study of galaxies during the earliest stages of the universe, made possible by its improved sensitivity, $7\times$ light-collecting area, and the broad imaging field of NIRCam (Rieke et al. 2005). In the early months of operation, several $z > 11$ galaxy candidates were identified (Naidu et al. 2022; Finkelstein et al. 2022; Harikane et al. 2023; Donnan et al. 2023; Atek et al. 2023a) as part of JWST’s Early Release Observations (ERO; Pontoppidan et al. (2022)), the Early Release Science (ERS) programs CEERS (Bagley et al. 2023) and Through the Looking GLASS (GLASS-JWST) programs (Treu et al. 2022). Many of the galaxy candidates identified in these early observations exceeded the previous distance record established by HST studies (Oesch et al. 2016). The discovery of early galaxy candidates has been further advanced by observational campaigns such as the JWST Advanced Deep Extragalactic Survey (JADES, Eisenstein et al. 2023a), the Next Generation Deep Extragalactic Exploratory Public (NGDEEP, Austin et al. 2023) survey, and the Prime Extragalactic Areas for Reionization and Lensing Science (PEARLS) project (Windhorst et al. 2023; Juodžbalis et al. 2023), which have utilized photometric techniques to identify $z \sim 9$ -16 galaxy candidates.

JADES is one of the most extensive initiatives in JWST’s first year of observation, dedicating 32 days of telescope time to the discovery and characterization of the most distant galaxies (Rieke et al. 2023a). The survey encompasses two deep fields, GOODS-South and GOODS-North, which have extensive legacy datasets provided by the Great Observatories Origins Deep Survey (GOODS; Dickinson et al. 2003; Giavalisco et al. 2004), and utilizes three instruments: NIRCam for imaging, NIRSpec for spectroscopy, and MIRI with an imaging and spectroscopy. JADES operates at two levels of survey depth: "Deep" and "Medium." The Deep survey is designed for in-depth characterization of fainter galaxies or detailed analysis of individual sources at higher signal-to-noise ratios, whereas the Medium survey facilitates a statistical analysis of the high-redshift galaxy population. Recently, Hainline et al. (2024) presents a impressive catalog of 717 candidate galaxies at redshifts $z > 8$, identified using deep imaging from JWST JADES program along with complementary data from FRESCO, JEMS, and HST. The candidates, selected through photometric redshifts, include many newly discovered sources—some potentially at redshifts up to $z \sim 18$.

In this paper, we report the detection of new $z > 11$ galaxy candidates using NIRCam observations taken across eight filters from the first year of the JADES survey in the GOODS-S and GOODS-N fields. The targets analyzed in this study are also included in the catalog released by JADES team, although with lower redshift estimates. Our analysis provides independent redshift measurements for these sources, based on refined photometry and an alternative modeling approach, offering a complementary perspective on their physical properties. We use two distinct codes EAZY (Brammer et al. 2008) and BAGPIPES (Carnall et al. 2018) for determining the redshifts of the candidates and their physical properties using SED fitting techniques to the photometric data. The format of the paper is as follows. In Section 2, we provide a detailed description of the observation and the photometric data reduction process, including photometric redshift estimation and dropout selection methods. In section 3, we detail the methodology for selecting galaxies at redshifts $z > 11$. In Section 4, we present the main results from our galaxy sam-

ple, including detailed descriptions, sizes, properties derived from SED fitting, and an analysis of systematic uncertainties and potential sources of contamination. In Section 5, we summarize our findings.

Throughout this paper, we adhere to the AB magnitude system (Oke & Gunn 1983) and cosmological parameters reported by Planck Collaboration et al. (2020): the Hubble constant $H_0 = 67.4 \text{ km s}^{-1} \text{ Mpc}^{-1}$, matter density parameter $\Omega_M = 0.315$, and dark energy density $\Omega_\Lambda = 0.685$.

2 OBSERVATION AND METHODS

The debut of the JWST in December 2021 opens up an unprecedented window into the study of the distant cosmos. Throughout the past year, a series of observation initiatives have been underway e.g., JADES (Hainline et al. 2024), CEERS (Finkelstein et al. 2015), GLASS (Castellano et al. 2022), NGDEEP (Leung et al. 2023) and many others. This paper centers on the analysis of data stemming from the JADES programs, with a particular focus on photometry.

2.1 JADES GOODS-S and GOODS-N observations

In this study, we investigate galaxy candidates identified through NIRCam imaging within the GOODS-S and GOODS-N field. GOODS-S encompasses observations conducted under Program 1180 led by PI Eisenstein from UT 2022-09-29 to 2022-10-10 (e.g., Bunker et al. 2023; Eisenstein et al. 2023a; Rieke et al. 2023b; Eisenstein et al. 2023b). Additionally, NIRCam parallels, covering 9.8 square arcminutes each, were observed during NIRSpec PID 1210 led by PI Ferruit from UT 2022-10-20 to 2022-10-24, positioned within and southwest of the JADES Medium footprint in GOODS-S. Further NIRCam observations (9.8 square arcminutes) parallel to NIRSpec PID 1286, also led by PI Ferruit, occurred from UT 2023-01-12 to 2023-01-13, situated northwest of the JADES Deep footprint in GOODS-S (e.g., Robertson et al. 2023; Tacchella et al. 2023; Hainline et al. 2024). The total survey area for JADES GOODS-S spans 67 square arcminutes, with 27 square arcminutes allocated for the JADES Deep program and 40 square arcminutes for the JADES Medium program. Utilizing filters F090W, F115W, F150W, F200W, F277W, F335M, F356W, F410M, and F444W ($\lambda = 0.8 - 5.0 \mu\text{m}$) for JADES Deep and the same filters without F335M for JADES Medium, these observations incorporate a minimum of six dither points per observation, with exposure times ranging from 14 to 60 ks. Consequently, the 5σ depths range from 3.4 to 5.9 nJy, with flux aperture sizes varying between 1.26 and 1.52 arcseconds.

The NIRCam GOODS-N program encompasses a total area of 58 square arcminutes. It’s split into two sections: the northwest (NW) covering 30.4 square arcminutes, and the southeast (SE) covering 27.6 square arcminutes. The NW part was observed as part of PID 1181 (PI: Eisenstein), using NIRCam as the main instrument. JADES guarantees a high level of pixel diversity across all filter bands, effectively mitigating flat-field inaccuracies, cosmic-ray interference, and other pixel-level issues. Figure 1 illustrates the GOODS-S and GOODS-N field covered by JADES survey, adopted from Hainline et al. (2024).

For this study, we utilized publicly available JADES data and reductions*. We specifically used NIRCam images from eight filters: F090W, F115W, F150W, F200W, F277W, F356W, F410M, and F444W. These images were processed with a pixel scale of 0.03''

* <https://archive.stsci.edu/hlsp/jades>

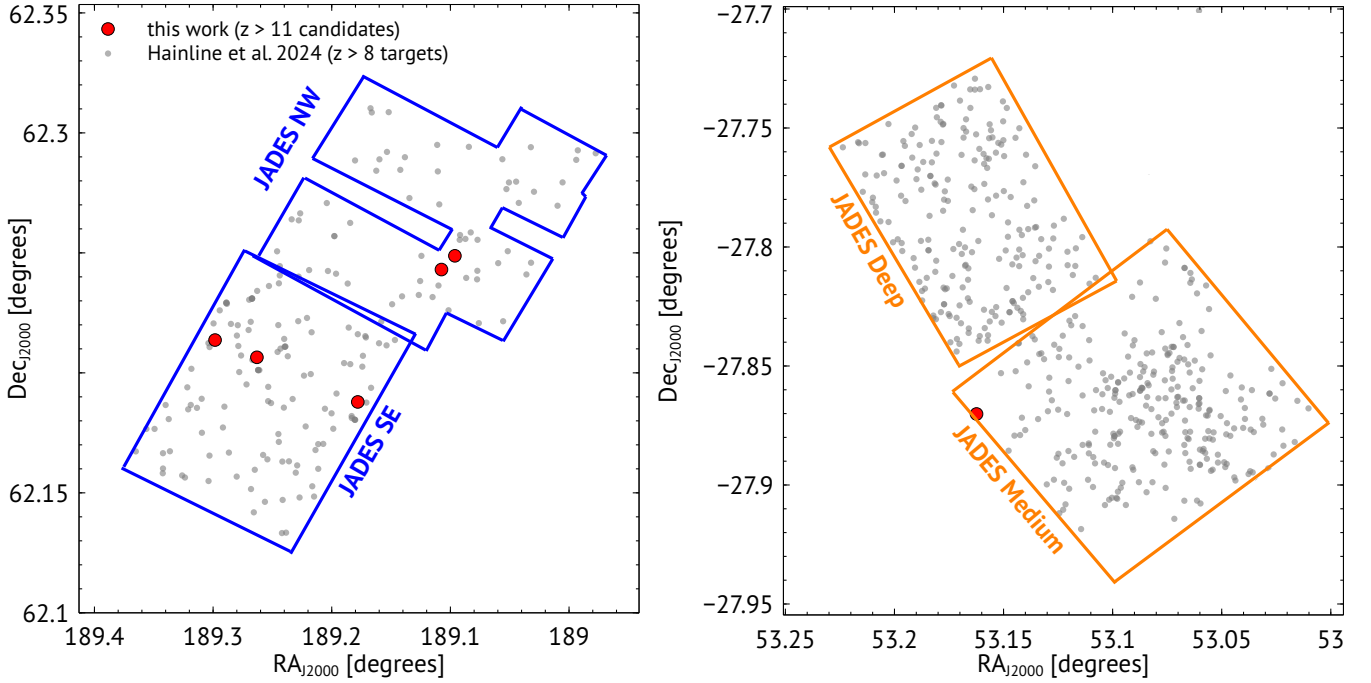


Figure 1. Left: Map displaying the GOODS-N field. The red data points represent our newly identified targets with $z > 11$ overlaid on the grey data points showing candidates with $z > 8$ listed in Hainline et al. (2024). Right: GOODS-S field. Our galaxy candidates with $z > 11$ were found in the JADES Medium GOODS-S region, with the grey data points again showing candidates with $z > 8$ from the same study.

per pixel. To identify sources in the images, we created a detection image by combining the F200W and F277W NIRCam bands using a weighted sum. We used image-segmentation tools from Photutils (Bradley et al. 2023a) and JWST data analysis tool notebooks[†] to identify sources with a SNR above 3 across five contiguous pixels. From this source catalog, we measured elliptical Kron aperture fluxes using Photutils.

We used a flexible Kron scale factor ($K = 1.5$) and a circularized radius six times larger than the Gaussian-equivalent elliptical sizes to ensure accurate measurements while masking any segmentation regions of neighboring sources (Bradley et al. 2023b; Hainline et al. 2024). The size of elliptical Kron aperture for each source was estimated by multiplying the Kron scale factor by the individual Kron radius.

We extracted and fitted to SED for each source adopting the Kron fluxes, as previous studies have demonstrated that measuring colors in small elliptical apertures accurately captures the colors of distant galaxies (Finkelstein et al. 2023; Bradley et al. 2023b). Additionally, we repeated a similar analysis using Kron apertures with a scale factor of 2.5. To correct for aperture effects, we estimated an aperture correction by comparing the total fluxes measured in the larger and smaller apertures for each source. This correction factor was then applied to the fluxes and uncertainties for all filters.

2.2 Photometric redshift estimation

We used EAZY-py, the Python implementation of the EAZY photometric redshift estimator code (Brammer et al. 2008), to derive the initial photometric redshifts. We utilize a set of 12

“tweak_fps_QSF_12_v3” templates derived from the Flexible Stellar Population Synthesis (FSPS) library (Conroy et al. 2009; Conroy & Gunn 2010). These templates include a range of galaxy types including star-forming, quiescent, and dusty and also include a range of star-formation histories, e.g., bursty, slowly rising, and slowly falling. Additionally, we utilize six newly developed templates from Larson et al. (2023), which were also applied by Adams et al. (2024) for deriving photometric redshifts of galaxies with $z > 7.5$. These additional templates were found to provide better photometric redshift estimation for $z > 9$ galaxies.

We utilized the $\chi^2(z)$ values generated by EAZY to compute a probability distribution, $P(z)$, assuming a uniform redshift prior. This distribution is given by the equation $P(z) = \exp[-\chi^2(z)/2]$, and it is normalized such that the integral of $P(z)$ over all redshifts equals 1.0. We vary redshifts in $0.1 < z < 20$, in steps of 0.01. Since the high-redshift luminosity function is still not well-constrained, we adopted a flat luminosity prior to prevent bias against the selection of bright high-redshift galaxies. Similar techniques were also adopted in several past JWST studies, such as Finkelstein et al. (2022); Bradley et al. (2023b).

3 SELECTION CRITERIA FOR HIGH-REDSHIFT CANDIDATES

We selected high-redshift galaxy candidates by combining EAZY-based SED fitting for photometric redshifts, signal-to-noise (SNR) criteria, as adopted in several past studies such as Salmon et al. (2020); Finkelstein et al. (2022, 2023); Bradley et al. (2023b); Leung et al. (2023); Atek et al. (2023a); Donnan et al. (2023); Hainline et al. (2024). We adopted photometric SNR criteria to ensure nondetections in filters bluer than $\text{Ly}\alpha$ and robust detections in filters redder than $\text{Ly}\alpha$ break. Finally, we visually inspect each galaxy candidates

[†] <https://jwst-docs.stsci.edu/jwst-post-pipeline-data-analysis>

for detector artifacts, diffraction spikes, and spurious noise close to detector edge.

Our selection criteria for identifying galaxy candidates with $z > 11$ are similar to the criteria adopted in [Finkelstein et al. \(2022\)](#) and [Bradley et al. \(2023b\)](#)-

(i) The best-fit photometric redshift, derived from EAZY SED fitting, must exceed 11 (i.e., $z > 11$).

(ii) An SNR of < 1.5 to ensure non-detections blueward of Lyman- α in all of the following filters F090W and F115W for $z < 13$. An additional F150W SNR of < 1.5 was also adopted for $z \geq 13$.

(iii) An SNR > 5.5 in at least two of the following filters: F150W, F200W, F277W, F356W, F410M, or F444W for $z < 13$ and F200W, F277W, F356W, F410M, or F444W for $z > 13$.

(iv) The integral of the EAZY posterior redshift probability ($P(z)$) of the galaxy being at $z > 11$ is greater than 70%, i.e. $\int_{z=11}^{\infty} P(z) dz > 0.7$.

(v) The angular separation between the candidates and any other nearby bright sources are at least $0.3''$, corresponding to 10 pixels.

In addition to the above criteria, we fitted each SED twice, first restricting EAZY maximum redshift to $z < 7$ (low-redshift) and then varying the redshift between $0 < z < 20$ (high redshift; see Figure 2–7). We estimated the disparity between the best-fit χ^2 for the low-redshift and high-redshift fit. For this work, we only consider $\Delta\chi^2 \geq 9$, ruling out the low-redshift model at $\geq 3\sigma$ significance ([Harikane et al. 2023](#)).

4 RESULTS AND DISCUSSION

Adopting the selection criteria and SED fitting method, we detect six new galaxy candidates at redshift $z > 11$ in the JADES GOODS-S and GOODS-N field. Below we discuss our primary results.

4.1 Galaxy sample with $z > 11$

Utilizing fits generated by EAZY, we identify six new candidates within the redshift range of $11 < z < 15$ across the GOODS-S and GOODS-N fields. Specifically, the five candidates are detected in GOODS-N, with the remaining two candidates detected in the GOODS-S field. Among the five candidates in GOODS-N, three are located in the southeastern sector, while the remaining two are located in its northwestern region. The two targets found in the GOODS-S field are specifically located within its medium region. Figure 1 illustrates the positions of these candidates in the GOODS-N and GOODS-S fields. Among the six candidates, three had redshifts between 11 and 12, while the remaining four showed best-fit photometric redshifts exceeding 12. Table 1 lists the newly identified candidates along with best-fit parameters from SED fitting.

All candidates are robust detections characterized by a precise high-redshift solution without any significant competing low-redshift alternatives, with ~ 70 -100% of their total probability concentrated within $\Delta z = 1$ around the best-fit solution. Similar quality classification criteria have been adopted in a recent *JWST* UNCOVER high-redshift survey ([Atek et al. 2023b](#)), where candidates meeting such criteria have been labeled as high-quality. Our sample targets the faint end of the luminosity distribution, covering a magnitude range of $m_{F277W} = 28.5$ and 30.4. Previous JADES surveys have documented systems with F277W AB magnitudes reaching as faint as 31.0 ([Hainline et al. 2024](#)). Figure 2, 3, 4, 5, 6, and 7 shows the $1.8'' \times 1.8''$ thumbnail images, best-fit SEDs from BAGPIPES and

EAZY, and the posterior redshift distributions. The red points represent the measured photometry. The best-fit favored high-redshift solutions (represented by black solid curves) have been shown along with the best-fit low-redshift solutions (represented by grey solid curves). The SED modeling and the physical properties of the galaxies derived from BAGPIPES fits are described in Section 4.3.

In our dataset, we identified three targets within the lowest redshift range in our sample, $11 < z < 12$ (EAZY determined), as illustrated in Figure 2, 3, and 4: JADES–53.16238-27.87016 (GOODS-S), JADES– 189.17805+62.18788 (GOODS-N), and JADES–189.09621+62.24877 (GOODS-N). In the observed $11 < z < 12$ galaxies, none exhibit substantial flux in the F115W images, thus classifying them as F115W dropout candidates. In the next higher redshift range, our survey identified three more candidate galaxies with photometric redshifts $12 < z < 15$ (EAZY determined): JADES–189.26307+62.20648 (GOODS-N), JADES– 189.29834 +62.21367 (GOODS-N), and JADES– 189.10753+62.24305 (GOODS-N). The corresponding thumbnail images are displayed in Figure 5, 6, and 7. JADES– 189.26307+62.20648 is categorized as an F115W dropout. The $z \geq 13$ targets, JADES– 189.29834+62.21367 and JADES–189.10753+62.24305 are both categorized as F150W dropouts.

4.2 Size of galaxies

We estimated the sizes of all 7 galaxies in our sample through the parametric fitting of the NIRCcam images using the Python package Photutils, an Astropy package for photometry and detection of astronomical sources ([Bradley et al. 2022](#)). We estimated the half-light radius for F277W filter using the Kron scale factor of 2.5, as adopted by [Bradley et al. \(2023b\)](#).

In Figure 8, we present the F277W half-light radii of our high-redshift galaxy candidates. The figure displays both the pixel size and the corresponding physical sizes (in kpc). The physical sizes were estimated using the photometric redshifts derived from BAGPIPES fits, as shown in Table 1. We find half-light radii ranging between 2.0 pixels to 2.7 pixels, corresponding to an angular spread between $0.06''$ and $0.081''$ (adopting pixel size of $0.03''$), with a median of $0.06''$. Given the F277W PSF full-width at half maximum of $0.088''$, and a radius of $0.044''$, all the galaxies are spatially resolved. The angular spreads translate to half-light radii ranging between 0.24 kpc to 0.34 kpc, with a median of 0.25 kpc for our galaxy candidates. These dimensions are in agreement with the rest-UV sizes reported in the GLASS survey, indicating a median half-light radius of 0.45 ± 0.13 kpc for $7 < z < 15$ galaxies in the F444W band ([Yang et al. 2022](#)), as well as with the CEERS survey, which found a median half-light radius of 0.46 kpc for $9 < z < 16$ galaxies in the F200W band ([Finkelstein et al. 2023](#)).

4.3 Physical Properties through SED fitting

To derive the physical properties of the identified galaxy candidates, we utilized the state-of-the-art Bayesian SED fitting code BAGPIPES ([Carnall et al. 2018](#)) to fit the observed SED. BAGPIPES generates complex model galaxy spectra and fits photometric and spectroscopic observations using nested sampling algorithm (e.g., nautilus sampler; [Dittmann 2024](#)), thereby generating posterior distributions of galaxy properties for each source in the sample. BAGPIPES is capable of modeling galaxies with various star formation histories (SFHs), including delayed- τ , constant, and bursts ([Lower et al. 2020](#)). The stellar population synthesis models adopted for this work are based on BC03 ([Bruzual & Charlot 2003](#)) version 2016. These models

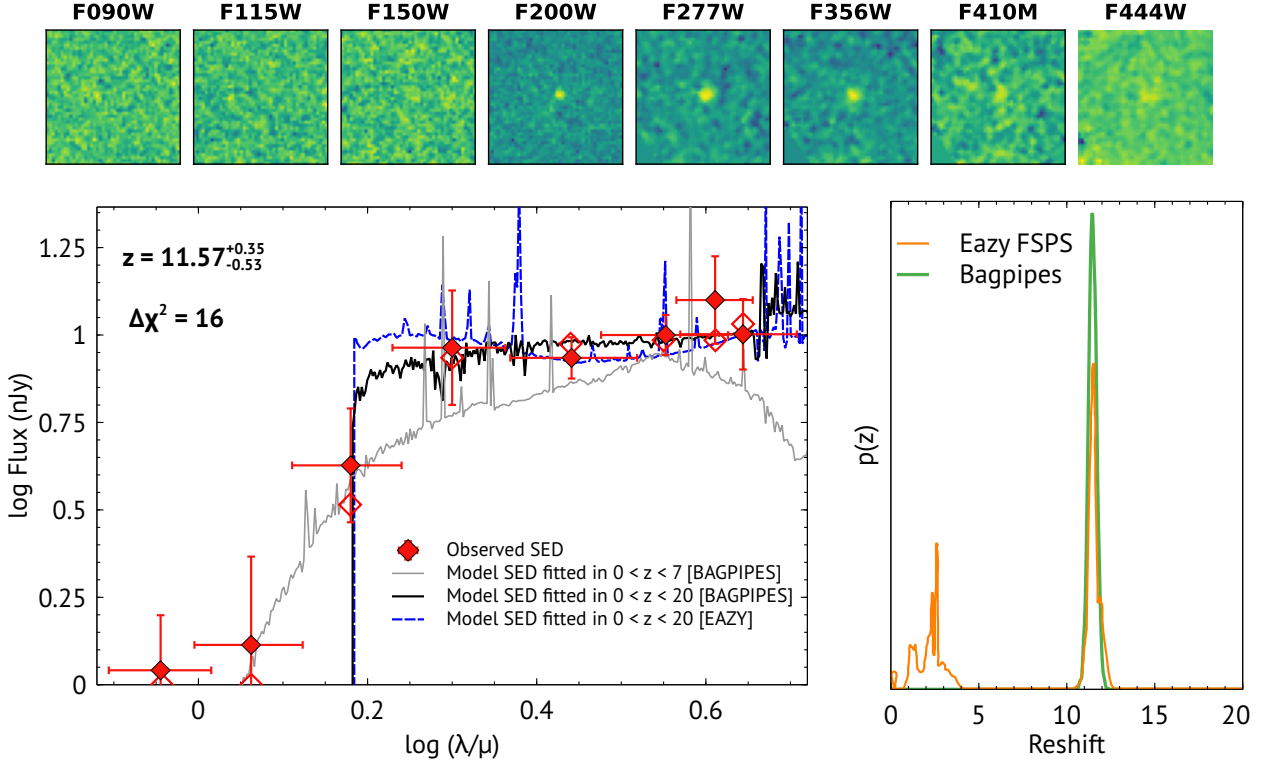


Figure 2. Thumbnail images for JADES– 53.16238 -27.87016. In each panel, the top rows display $1.8'' \times 1.8''$ image cutouts for the 8 JWST filters. The bottom-left panels represent the observed photometry in red data points along with their corresponding 1σ uncertainties. The best-fit SEDs from BAGPIPES for the preferred high-redshift solution are shown as a black solid curve, while the corresponding SEDs for the low-redshift solution are represented as a solid grey curve. Open red diamonds represent best-fit BAGPIPES model photometry for high-redshift solution. The best-fit SEDs with EAZY for the preferred high-redshift solution are shown with blue dashed curve. The redshift range displayed in the plot was determined using EAZY. In addition, the posterior probability distributions, $P(z)$, for photometric redshift solutions is displayed with the orange curves in the bottom-right panels.

assume the Kroupa (2002) initial mass function (IMF) and include nebular line and continuum emission using CLOUDY (Chatzikos et al. 2023). For this study, we selected a delayed- τ SFH (where $\text{SFR}(t) \propto te^{-t/\tau}$) following Morales et al. (2024), known for its effectiveness in modeling the majority of the stellar population and accurately estimating stellar masses (Ciesla et al. 2017).

We modified the BAGPIPES source code to expand the default redshift range from $z = 0 - 10$ to $z = 0 - 20$, ensuring consistency with the EAZY-py results used to select the galaxy sample (Section 2.2). The BAGPIPES SED-fitting was conducted over a wide range of parameter space. We vary τ within 0.1 and 14 Gyr, stellar masses within $\log(M_*/M_\odot) = 4$ and 13, and \log of metallicities ($\log Z/Z_\odot$) within 0.005 and 2.5. The logarithm of the ionization parameter ($\log U$), for accounting nebular line and continuum emission, was allowed to vary within -4 and -2 . For this work we adopted Calzetti dust attenuation curve to reduce the number of free parameters in our fits (Calzetti et al. 2000). We let the dust extinction A_V vary within 0 and 4. Additionally, we introduced a multiplicative factor ($1 < \eta < 2$) to the dust model to address birth-cloud dust attenuation, which typically doubles around H II regions compared to the general ISM within the galaxy’s first 10 Myr (Bradley et al. 2023b). To account for this, we capped the maximum age of the birth-cloud at 0.01 Gyr (Giménez-Arteaga et al. 2023). The age parameter was allowed to range from 1 Myr to the age of the Universe. Following a similar approach to the EAZY fitting, we conducted two fits of the observed photometry with BAGPIPES. Initially, we constrained the redshift range to $z < 7$. Then, we performed another fitting while allowing

the redshift to vary between 0.1 and 20. Figure 2, 3, 4, 5, 6, and 7 display the best-fit model SEDs obtained from the BAGPIPES fitting, accompanied by the corresponding $\Delta\chi^2$ values.

The physical parameters extracted from the BAGPIPES fittings are detailed in Table 1. Among these parameters, the inferred intrinsic stellar masses exhibit a range approximately from $\log M_*/M_\odot \sim 7.75$ to 8.75, while the corresponding star formation rates (SFRs) span from around ~ 0.9 to $5.1 M_\odot/\text{yr}$. Additionally, the specific star formation rates (sSFRs), quantified as $\log \text{sSFR}/\text{Gyr}$, vary within the range of approximately ~ 0.95 to 1.46. Notably, similar sSFRs have been found for galaxy candidates at redshifts $z > 8$ in Bradley et al. (2023b).

Furthermore, the inferred ages for all galaxy candidates within our sample indicate younger stellar populations, spanning a range of approximately 80 to 240 million years, similar to the ages found in earlier photometric detections of galaxies at $z \sim 10$ (Laporte et al. 2021; Bradley et al. 2023b). Regarding dust extinction, the best-fit values of A_V range from 0.02 to 0.45. These values are consistent with those found in $z = 9 - 16$ galaxies in the NGDEEP survey (Morales et al. 2024), which were also fitted using BAGPIPES and exhibited A_V values between 0.04 and 1.03. These findings collectively contribute to a deeper understanding of the stellar populations and dust properties within the observed galaxy sample.

Recent studies also points to bursty star formation histories in galaxies at $z > 6$ compared to their lower-redshift counterparts, with episodic bursts temporarily enhancing the luminosity of low-mass galaxies due to the rapid formation of massive O stars (Looser et al.

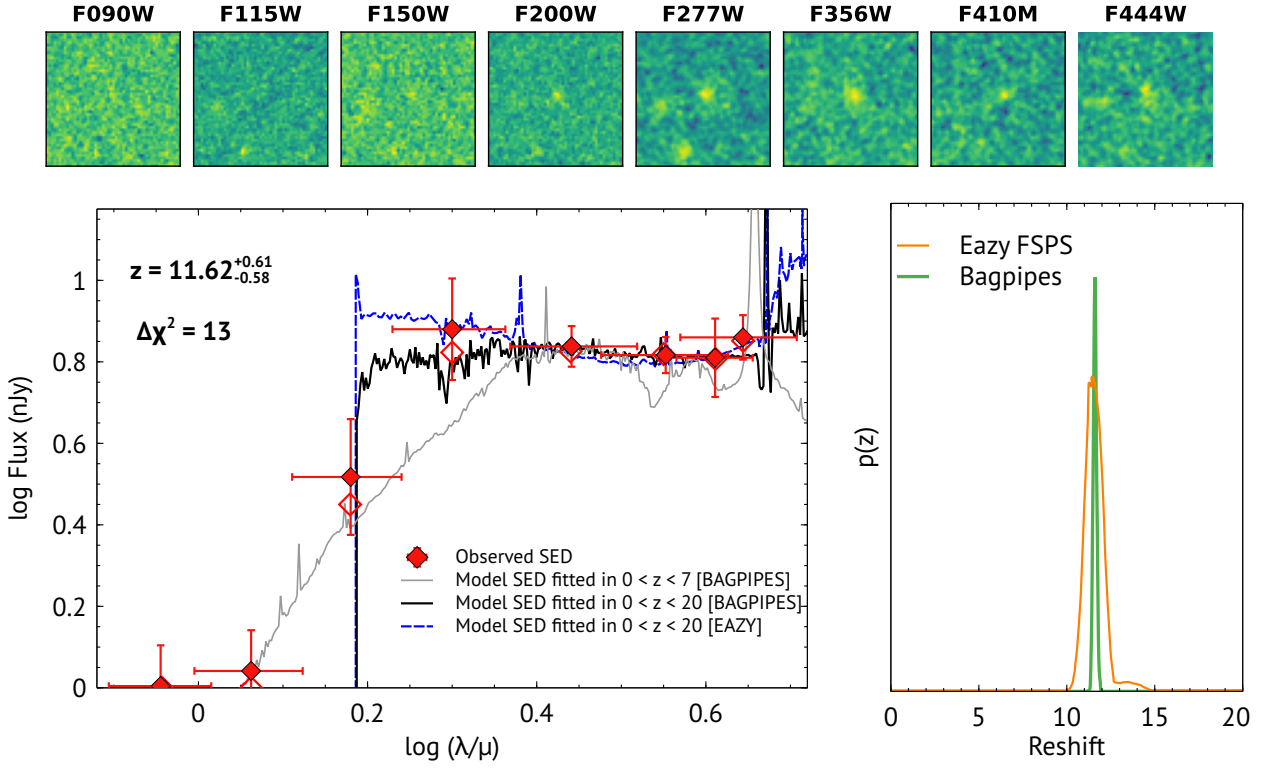


Figure 3. Same as Figure 2, but for JADES- 189.17805+62.18788.

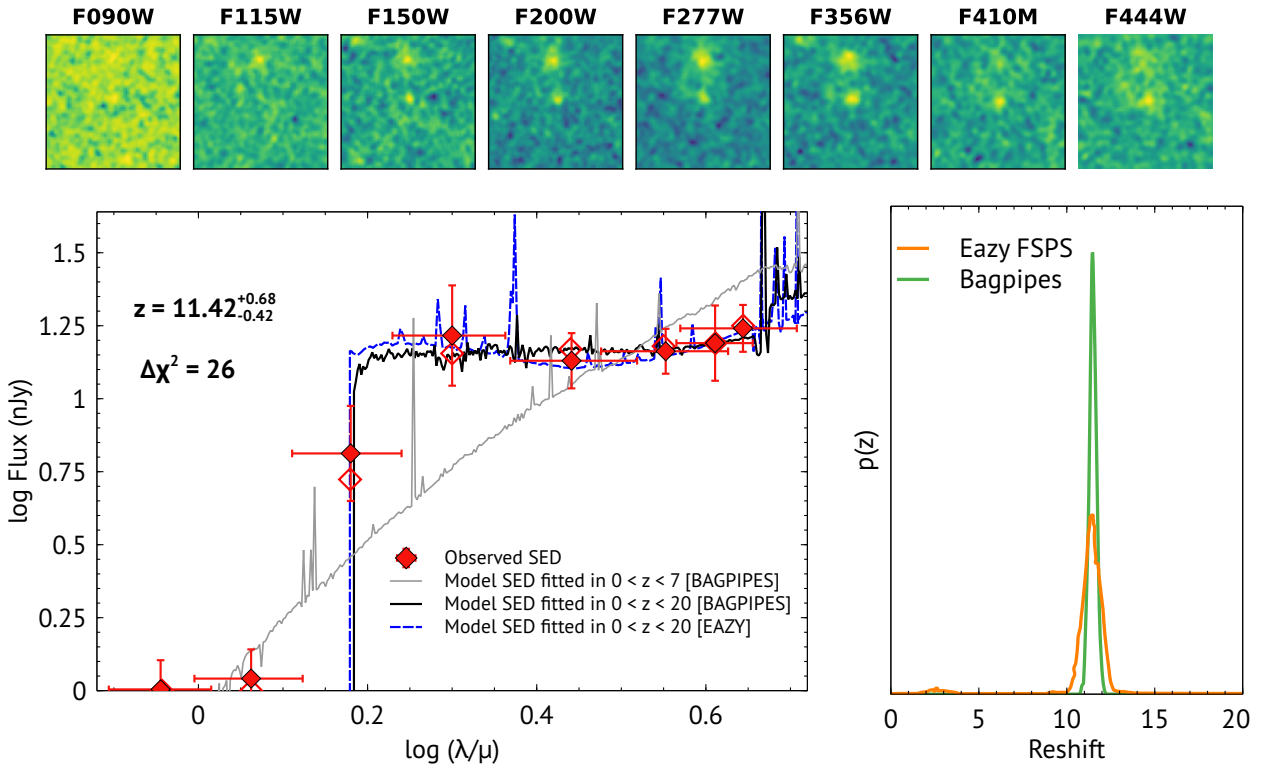


Figure 4. Same as Figure 2, JADES- 189.09621+62.24877

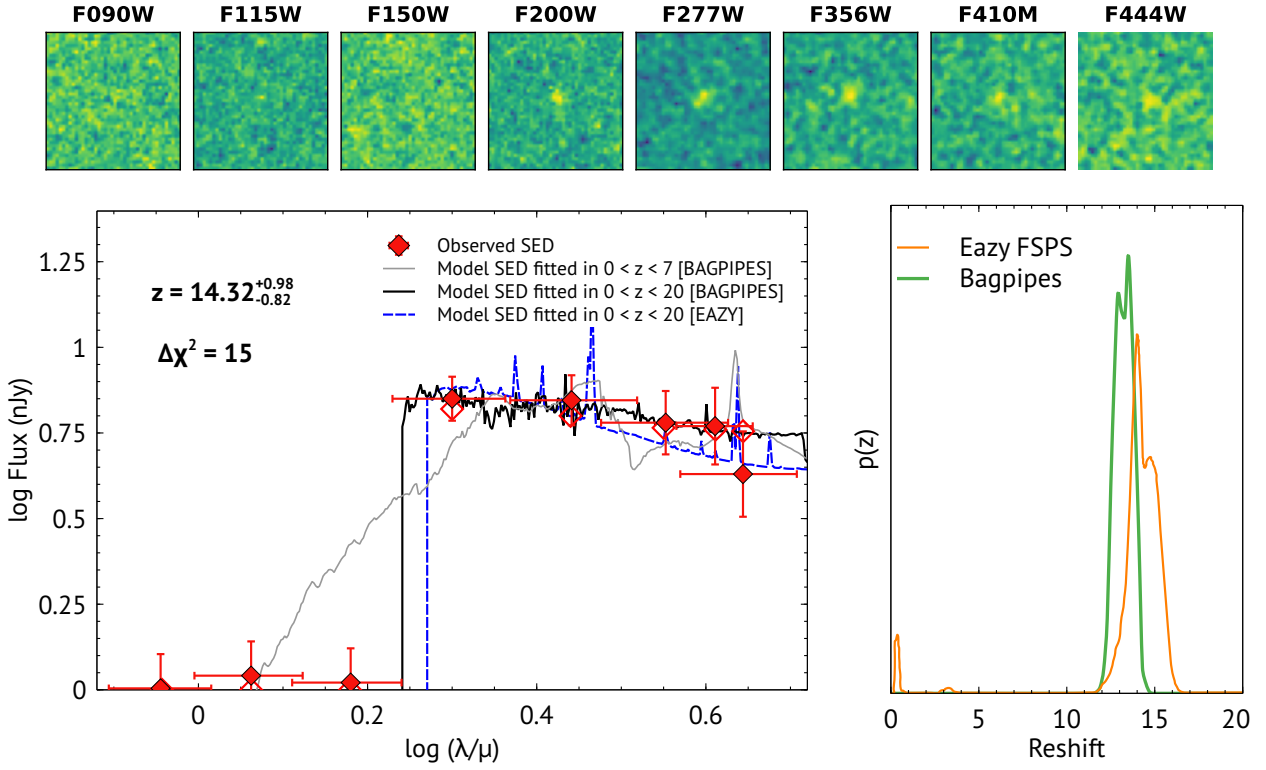


Figure 5. Same as Figure 2, but for JADES- 189.29834 +62.21367

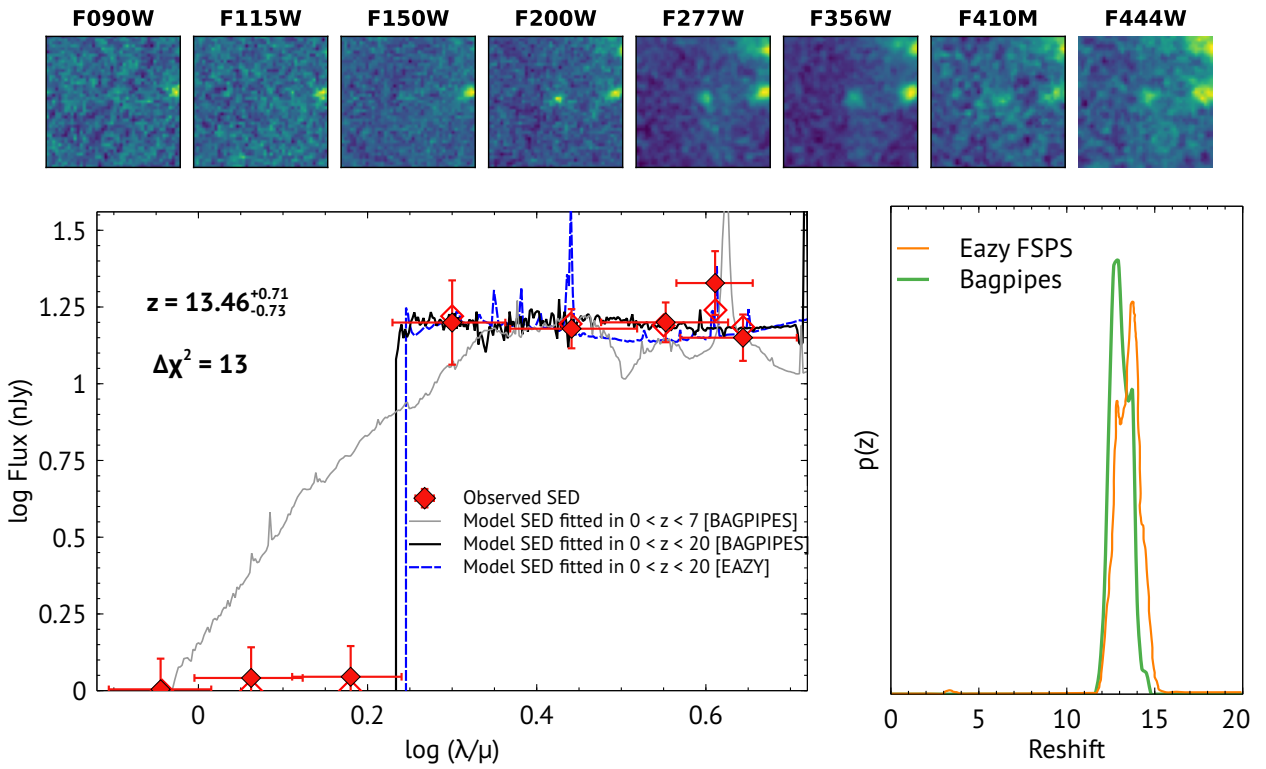


Figure 6. Same as Figure 2, but for JADES- 189.10753+62.24305.

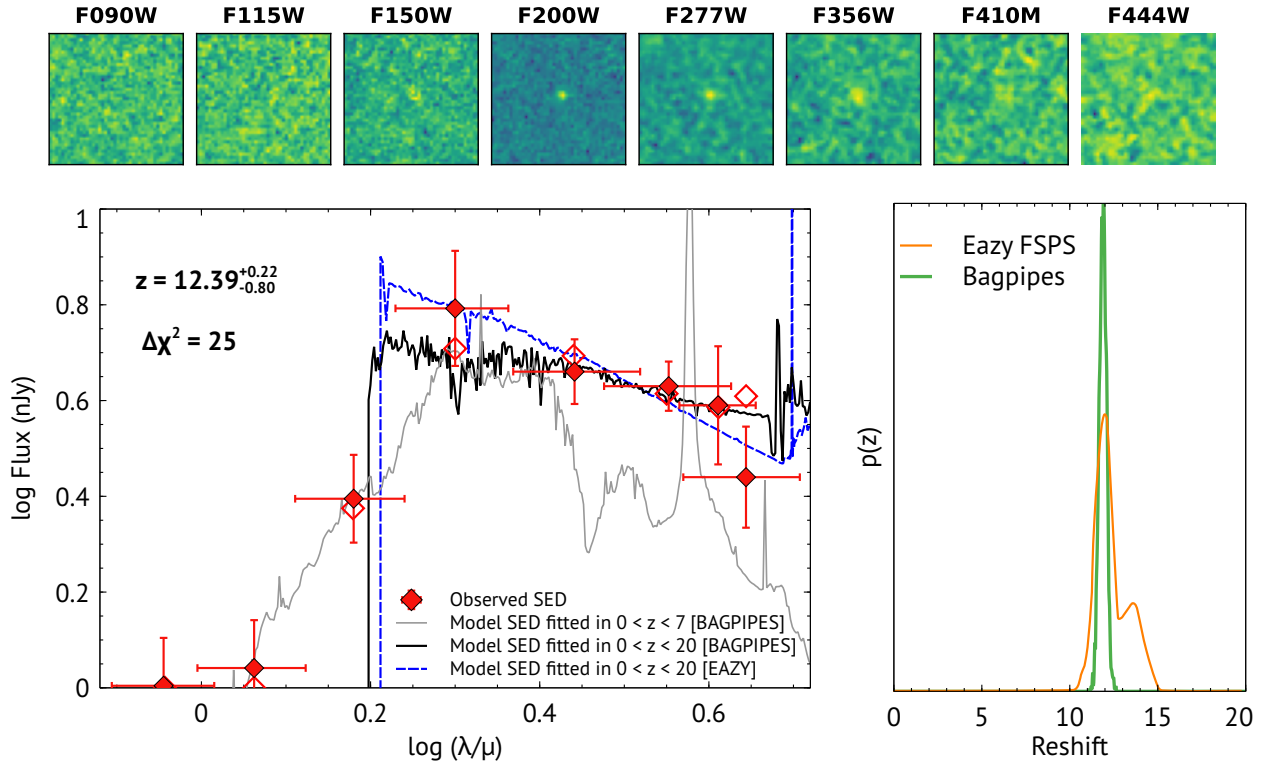


Figure 7. Same as Figure 2, but for JADES– 189.26307+62.20648.

Table 1. Photometric redshifts from EAZY and BAGPIPES SED fitting, along with physical properties of the galaxy candidates estimated with BAGPIPES. Best-fit parameters correspond to delayed- τ star formation history model, as presented in Figures 2–7. Errors are estimated with 1σ uncertainties.

* – Redshifts as listed in JADES catalog.

† – Best-fit redshifts from EAZY fit within $0 < z < 20$.

†† – Best-fit redshifts from BAGPIPES fit within $0 < z < 20$.

RA (deg)	DEC (deg)	z_{JADES}^*	z_{EAZY}^\dagger (z_{-a})	$z_{\text{Bagpipes}}^{\dagger\dagger}$	m_{F277} (AB)	$\Delta\chi^2$ (68%)	$P(z)$	$\log(M_*/M_\odot)$	SFR (100 Myr) ($M_\odot\text{yr}^{-1}$)	SFR (10 Myr) ($M_\odot\text{yr}^{-1}$)	Age (Myr)	A_v	r_{hl} (pix/arcsec)
GOODS-S													
53.16238	-27.87016	3.5	$11.57^{+0.35}_{-0.53}$	$11.46^{+0.24}_{-0.23}$	28.8 ± 0.1	16	0.7	$8.59^{+0.19}_{-0.29}$	$4.2^{+2.2}_{-1.1}$	$2.4^{+1.4}_{-0.5}$	200^{+130}_{-120}	$0.45^{+0.15}_{-0.15}$	2.1 ± 0.1
GOODS-N													
189.17805	62.18788	2.91	$11.62^{+0.61}_{-0.58}$	$11.5^{+0.1}_{-0.1}$	30.4 ± 0.1	13	0.9	$8.25^{+0.17}_{-0.27}$	$1.8^{+0.7}_{-0.3}$	$1.7^{+0.7}_{-0.5}$	230^{+100}_{-140}	$0.22^{+0.12}_{-0.11}$	2.1 ± 0.2
189.26307	62.20648	9.51	$12.39^{+0.22}_{-0.80}$	$11.89^{+0.20}_{-0.22}$	29.0 ± 0.1	25	0.9	$7.75^{+0.26}_{-0.31}$	$0.9^{+0.2}_{-0.2}$	$0.85^{+0.20}_{-0.13}$	120^{+80}_{-70}	$0.10^{+0.07}_{-0.03}$	2.0 ± 0.3
189.29834	62.21367	4.93	$14.32^{+0.98}_{-0.82}$	$13.5^{+0.5}_{-0.6}$	30.2 ± 0.2	15	0.9	$7.93^{+0.23}_{-0.45}$	$1.3^{+0.3}_{-0.3}$	$1.25^{+0.3}_{-0.22}$	136^{+120}_{-100}	$0.06^{+0.08}_{-0.04}$	2.0 ± 0.2
189.10753	62.24305	3.42	$13.46^{+0.71}_{-0.73}$	$13.01^{+0.65}_{-0.52}$	29.4 ± 0.1	13	0.9	$8.62^{+0.12}_{-0.20}$	$4.2^{+1.3}_{-0.7}$	$4.33^{+1.58}_{-0.99}$	190^{+90}_{-80}	$0.23^{+0.09}_{-0.10}$	2.7 ± 0.3
189.09621	62.24877	2.93	$11.42^{+0.68}_{-0.42}$	$11.5^{+0.2}_{-0.2}$	29.6 ± 0.2	26	0.9	$8.75^{+0.17}_{-0.25}$	$5.1^{+2.2}_{-1.2}$	$4.86^{+1.81}_{-1.18}$	240^{+100}_{-140}	$0.40^{+0.15}_{-0.13}$	2.6 ± 0.4

2025). At higher redshifts ($z > 10$), several theoretical models have demonstrated that an evolving burstiness can naturally explain the unexpectedly high abundance of bright galaxies detected by JWST in the $z = 10 - 14$ range (Ferrara et al. 2023). These models suggest that short, intense episodes of star formation—dominate the early buildup of stellar mass in the first few hundred million years after the Big Bang. Therefore, to further assess the impact of star formation history assumptions, we re-derived the stellar mass, redshift, and SFR

of our galaxy candidates using a bursty SFH model implemented in BAGPIPES. We implemented the same fitting method as discussed earlier for the delayed- τ SFH model. Figure 9 presents a comparison between the delayed- τ and bursty SFH results. The derived stellar masses and redshifts are consistent across both models. However, in 4 out of 6 galaxy candidates, the SFRs inferred from the bursty SFH are significantly higher than those obtained with the delayed- τ model.

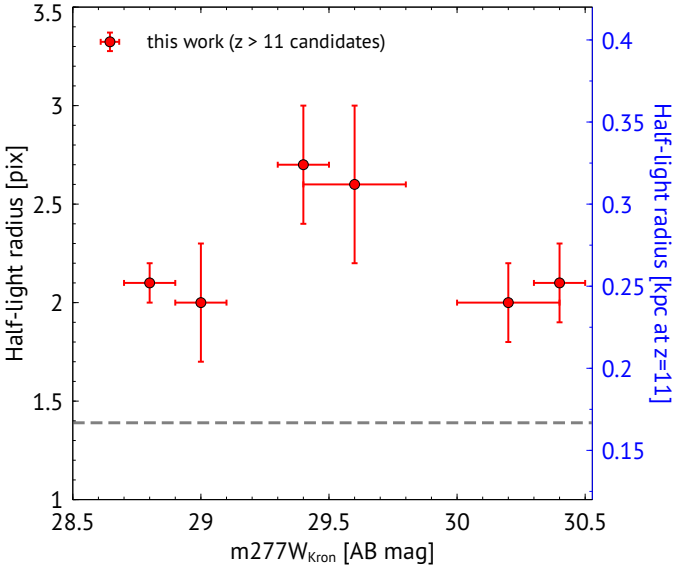


Figure 8. Half-light radius vs. AB Kron magnitude in F277W filter. Red data points show the Half-light radius of our sample galaxy candidates with 1σ uncertainties. A secondary y-axis for half-light radius in kpc (scaled at $z = 11$) is shown on the right side. The grey dashed line displays the F277W PSF FWHM in pixels (1.397 pixels).

4.4 SFR vs. stellar mass relation

Noeske et al. (2007) and Elbaz et al. (2007) demonstrated that galaxies at $z \sim 1$ exhibit a tight correlation between star formation rate and stellar mass, with a scatter of 0.2 dex and a rough proportionality characterized by a logarithmic slope of 0.9. This proportionality is similarly observed at $z \sim 0$ using data from the Sloan Digital Sky Survey (Elbaz et al. 2007). However, the normalization at $z \sim 0$ is lower, reflecting the overall decline in cosmic star formation rate density over time. This tight correlation between SFR and stellar mass, known as the main sequence (MS) of star formation, has been extensively documented in the literature (e.g., Daddi et al. 2007; Noeske et al. 2007; Elbaz et al. 2007). This relationship has been observed in high redshifts, with its evolution parametrized up to $z \sim 6$ (e.g., Speagle et al. 2014). However, establishing the MS at high redshifts poses significant challenges due to various systematic uncertainties and selection effects inherent in compiling representative galaxy samples (e.g., Grazian et al. 2015; Förster Schreiber & Wuyts 2020; Furtak et al. 2021, 2023). In order to probe the poorly understood Universe at $z \gtrsim 10$, which is beginning to unfold with the advent of the JWST, we investigate the SFR–stellar mass (SFR– M_*) relation within our sample and compare it with previous studies.

In Figure 10, we present the distribution of our galaxy sample in the SFR– M_* plane, where the physical properties are derived using the BAGPIPES code. For each galaxy, we compute the SFR averaged over both the most recent 100 Myr and 10 Myr time intervals, allowing us to assess recent star formation activity on different timescales. In the left panel of Figure 10, we compare our 100 Myr-averaged SFR– M_* distribution to that of galaxies identified in the NGDEEP survey spanning redshifts $z = 9–16$ (Morales et al. 2024). Their analysis employs a methodology comparable to ours, using SED fitting to estimate physical properties from deep photometric data, including BAGPIPES code and 100 Myr-averaged SFR. This comparison provides a useful benchmark against another photometrically selected high-redshift sample. Observationally, it has been shown that SFRs derived from dust attenuation corrected $H\beta$ flux are strongly corre-

lated with SFRs averaged over the most recent $\lesssim 10$ Myr (Guo et al. 2016; Nakajima et al. 2023). Motivated by this, we compare our 10 Myr-averaged SFR– M_* relation to that of galaxies from the CEERS survey at $z = 3–10$, for which SFRs were measured using NIR-Spec spectroscopy (Nakajima et al. 2023). These spectroscopically confirmed galaxies provide an independent check on our photometric estimates of SFR– M_* distribution over a broad redshift range. In both comparisons, we overlay the star-forming main sequence at $z \sim 6$ as reported by Salmon et al. (2015) and Popesso et al. (2023), shown as reference lines in each panel. Overall, our results are in good agreement with previous studies, supporting the robustness of our derived stellar masses and SFRs across different SFH assumptions and timescales.

4.5 Limitations of SED-fitting method and contaminations

We solely utilize SED fitting tool BAGPIPES to derive the physical properties of our high-redshift sample of galaxies. Though the effectiveness and flexibility of BAGPIPES code has been shown in many previous studies, such as Bradley et al. (2023b); Morales et al. (2024), the physical properties of high-redshift galaxies derived from BAGPIPES may be affected by several limitations and contaminations.

Analyzing SEDs through fitting broadband photometry, which mainly captures the rest-frame UV emissions of potential high-redshift galaxies is one of the limitations of our analysis. This wavelength range primarily highlights massive, short-lived stars within a galaxy, which might not represent the majority of its stellar mass. Due to the limited availability of rest-frame optical photometry, SED fitting is expected to underestimate stellar masses. Specifically, Furtak et al. (2021) demonstrated that relying solely on UV photometry can result in an underestimation of stellar masses by up to 0.6 dex. Stellar masses can be accurately derived from the UV continuum only if a galaxy is $\lesssim 10$ Myr old, which is the typical lifetime of massive stars. Beyond this age, accurate stellar mass determination requires continuum detection redward of the Balmer break. Furthermore, relying solely on rest-frame UV photometry can create ambiguities between stellar mass, SFR, and age, as noted by Furtak et al. (2023). To confirm if galaxies at $z \gtrsim 10$ possess an evolved stellar population, as suggested by recent simulations (Mason et al. 2023), JWST/NIRCam imaging at wavelengths $\lambda \lesssim 5\mu\text{m}$ should be supplemented with future observations targeting the rest-frame optical emission of these very high-redshift galaxies.

Another constraint of our analysis arises from assuming a Lyman continuum (LyC) escape fraction of $f_{\text{esc}} = 0$ as per BAGPIPES. However, the LyC escape fraction significantly influences the shape of the SED through its impact on nebular emission. Specifically, it attenuates both nebular line and continuum emissions, resulting in a bluer SED and a steeper UV slope (Plat et al. 2019). Observations of known LyC leakers at low redshifts reveal a clear correlation between UV slope and LyC escape fraction (Chisholm et al. 2022). Although recent studies suggest low $f_{\text{esc}}(\text{LyC})$ values of $\lesssim 10\%$ in galaxies at $z > 7$ (Witten et al. 2023), it remains essential to account for the effect of $f_{\text{esc}}(\text{LyC})$ in highly star-forming primeval galaxies in the early Universe. This consideration is paramount as it could pose challenges in replicating the extremely blue UV slopes observed in some galaxies detected by JWST at $z > 10$. Therefore, future investigations aimed at accurately determining physical parameters of high-redshift galaxies through SED-fitting must incorporate templates that allow for $f_{\text{esc}} > 0$.

The primary source of contamination in broad-band photometry of high-redshift galaxy samples often stems from faint low-redshift galaxies with strong line emission or Balmer breaks. Although our

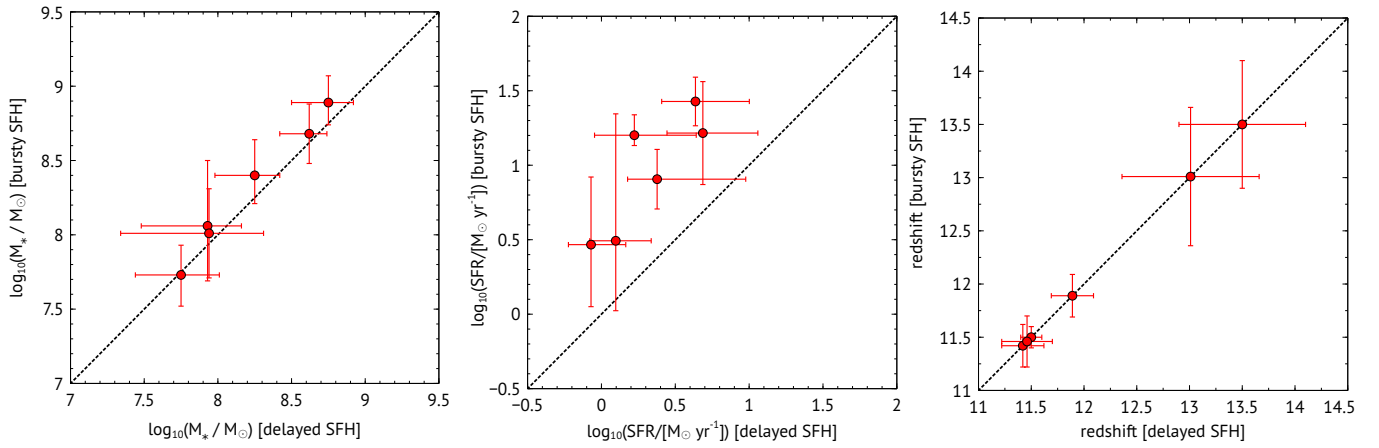


Figure 9. Comparison of derived stellar masses, star-formation rates, and redshifts for the newly identified galaxy candidates using delayed- τ and bursty star formation history models. Star formation rates are averaged over the last 100 Myr.

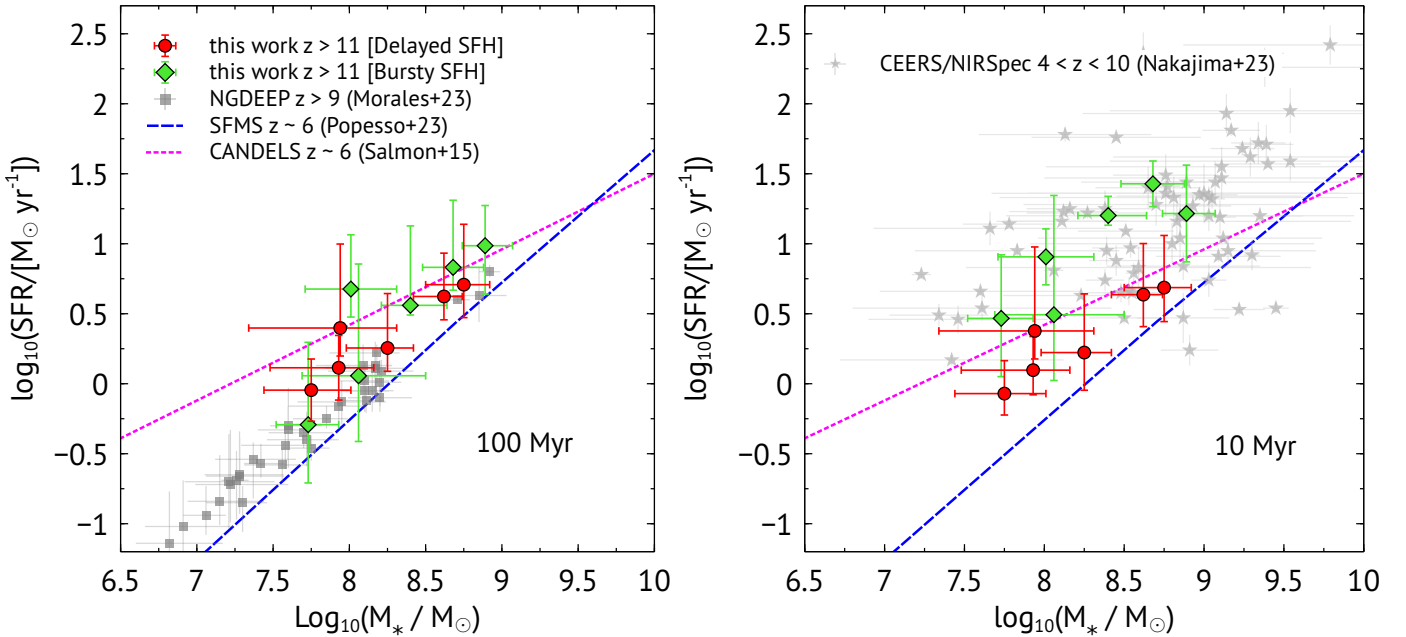


Figure 10. Distribution of stellar mass versus star formation rate (SFR) for the photometric galaxy sample analyzed in this study. Left: SFRs averaged over the past 100 Myr for newly identified galaxy candidates, derived using delayed (red) and bursty (green) star formation history (SFH) models. Grey squares represent NGDEEP galaxies from [Morales et al. \(2024\)](#), with SFRs also derived from photometry. Right: SFRs averaged over the past 10 Myr for the same galaxy candidates, using the same SFH models (delayed in red, bursty in green). Grey stars show CEERS galaxies with SFRs inferred from $H\beta$ luminosity, compiled by [Nakajima et al. \(2023\)](#). In both panels, the star-forming main sequence at $z \sim 6$ is shown for reference: the blue dashed line represents the relation from [Popesso et al. \(2023\)](#), and the magenta dotted line from [Salmon et al. \(2015\)](#).

selection criteria for high-redshift samples are meticulously crafted to mitigate contamination from lower-redshift interlopers, the potential still exists for some of our candidates to reside at lower redshifts. Spectroscopic confirmation is imperative to accurately determine the redshifts of these candidates.

5 CONCLUSION

In this paper, we present the outcomes of our investigation aimed at identifying $z > 11$ galaxy candidates in the JWST NIRCcam obser-

vations of JADES GOODS-S and GOODS-N fields. We undertake an extensive data reduction process that involves several custom procedures. We use two distinct codes, EAZY and BAGPIPES, for photometric redshift determination and investigating the properties of these galaxies. We detect six $z > 11$ candidate galaxies distributed as follows: three candidates between $11 < z < 12$, and four candidates between $12 < z < 15$. All candidates are robust high-redshift detections with 70-100% of their probability within $\Delta z = 1$, meeting the classification ‘high-quality’ used in a recent JWST UNCOVER high-redshift survey ([Atek et al. 2023b](#)). The detection of these young galaxies spans a diverse range of magnitudes, with F277W AB Kron

magnitude values between 28.5 and 30.4, consistent with previous JADES surveys, which achieved detections as faint as AB mag 31.0 for the young galaxies at redshifts greater than 10 (Hainline et al. 2024).

To assess the physical properties of the galaxies, we perform SED fitting to the photometric data of these galaxies using BAGPIPES. We obtain measurements for stellar mass, SFRs averaged over the last 100 Myr and 10 Myr, dust content, and mass-weighted age, which are listed in Table 1. We find the intrinsic stellar masses of our galaxy candidates to vary within the range of $\log(M_*/M_\odot) = 7.75$ to 8.75. Their SFRs span between 0.9 and $5.1 M_\odot \text{yr}^{-1}$, while their sSFRs, quantified as $\log \text{sSFR}/\text{Gyr}$, range from 0.95 to 1.46. The mass-weighted ages of these galaxies range between 80 to 240 Myr, with their dust content varying between $A_V = 0.02$ and 0.45. We present the distribution of galaxy candidates on the stellar mass versus star formation rate plane and compare our findings, which closely align with those of previous surveys (Nakajima et al. 2023; Morales et al. 2024; Curti et al. 2024).

Previous studies have demonstrated that photometry is a reliable method for determining galaxy properties. When used in conjunction with SED fitting codes such as BAGPIPES, photometry can reliably estimate photometric redshifts, stellar masses, and star formation rates (Duan et al. 2024). However, slight differences that may arise between properties derived from spectroscopy and those obtained through photometry must be considered when calibrating an absolute scale for the star formation rates and stellar mass histories of galaxies. Moving forward, JWST/NIRSpec observations will be essential for confirming these early galaxies, allowing for a more detailed analysis of their intrinsic properties.

ACKNOWLEDGEMENTS

We thank the anonymous referee for their helpful comments and suggestions. This work is based on observations made with the NASA/ESA/CSA James Webb Space Telescope. We thank Dr. Daniel Eisenstein for the helpful discussion on JWST/JADES data. We acknowledge support by NASA Chandra grant GO5-26101X 16619404 and NASA ADAP Grant 80NSSC21K0637.

DATA AVAILABILITY

The data underlying this article will be shared on reasonable request to the corresponding author.

REFERENCES

Adams N. J., et al., 2024, *ApJ*, 965, 169
 Atek H., et al., 2023a, *MNRAS*, 519, 1201
 Atek H., et al., 2023b, *MNRAS*, 524, 5486
 Austin D., et al., 2023, *ApJ*, 952, L7
 Bagley M. B., et al., 2023, *ApJ*, 946, L12
 Barkana R., Loeb A., 2001, *Phys. Rep.*, 349, 125
 Beckwith S. V. W., et al., 2006, *AJ*, 132, 1729
 Bhatawdekar R., Conselice C. J., Margalef-Bentabol B., Duncan K., 2019, *MNRAS*, 486, 3805
 Bolzonella M., Miralles J. M., Pelló R., 2000, *A&A*, 363, 476
 Bouwens R. J., et al., 2011, *ApJ*, 737, 90
 Bouwens R. J., et al., 2015, *ApJ*, 803, 34
 Bouwens R. J., et al., 2021, *AJ*, 162, 47
 Bradley L., et al., 2022, *astropy/photutils*: 1.5.0, doi:10.5281/zenodo.6825092

Bradley L., et al., 2023a, *astropy/photutils*: 1.10.0, doi:10.5281/zenodo.1035865
 Bradley L. D., et al., 2023b, *ApJ*, 955, 13
 Brammer G. B., van Dokkum P. G., Coppi P., 2008, *ApJ*, 686, 1503
 Bromm V., Larson R. B., 2004, *ARA&A*, 42, 79
 Bromm V., Yoshida N., 2011, *ARA&A*, 49, 373
 Bruzual G., Charlot S., 2003, *MNRAS*, 344, 1000
 Bunker A. J., et al., 2023, *arXiv e-prints*, p. arXiv:2306.02467
 Calzetti D., Armus L., Bohlin R. C., Kinney A. L., Koornneef J., Storchi-Bergmann T., 2000, *ApJ*, 533, 682
 Carnall A. C., McLure R. J., Dunlop J. S., Davé R., 2018, *MNRAS*, 480, 4379
 Castellano M., et al., 2022, *ApJ*, 938, L15
 Chatzikos M., et al., 2023, *Rev. Mex. Astron. Astrofis.*, 59, 327
 Chisholm J., et al., 2022, *MNRAS*, 517, 5104
 Ciesla L., Elbaz D., Fensch J., 2017, *A&A*, 608, A41
 Coe D., et al., 2019, *ApJ*, 884, 85
 Conroy C., Gunn J. E., 2010, FSPS: Flexible Stellar Population Synthesis, Astrophysics Source Code Library, record ascl:1010.043
 Conroy C., Gunn J. E., White M., 2009, *ApJ*, 699, 486
 Curti M., et al., 2024, *A&A*, 684, A75
 Daddi E., et al., 2007, *ApJ*, 670, 156
 Dickinson M., Giavalisco M., GOODS Team 2003, in Bender R., Renzini A., eds, *The Mass of Galaxies at Low and High Redshift*. p. 324 (arXiv:astro-ph/0204213), doi:10.1007/10899892_78
 Dittmann A., 2024, *The Open Journal of Astrophysics*, 7, 79
 Donnan C. T., et al., 2023, *MNRAS*, 518, 6011
 Duan Q., Conselice C. J., Li Q., Harvey T., Austin D., Ormerod K., Trussler J., Adams N., 2024, *MNRAS*, 529, 4728
 Eisenstein D. J., et al., 2023a, *arXiv e-prints*, p. arXiv:2306.02465
 Eisenstein D. J., et al., 2023b, *arXiv e-prints*, p. arXiv:2310.12340
 Elbaz D., et al., 2007, *A&A*, 468, 33
 Ellis R. S., et al., 2013, *ApJ*, 763, L7
 Fan X., Carilli C. L., Keating B., 2006, *ARA&A*, 44, 415
 Ferrara A., Pallottini A., Dayal P., 2023, *MNRAS*, 522, 3986
 Finkelstein S. L., et al., 2015, *ApJ*, 810, 71
 Finkelstein S. L., et al., 2022, *ApJ*, 940, L55
 Finkelstein S. L., et al., 2023, *ApJ*, 946, L13
 Förster Schreiber N. M., Wuyts S., 2020, *ARA&A*, 58, 661
 Furtak L. J., Atek H., Lehnert M. D., Chevallard J., Charlot S., 2021, *MNRAS*, 501, 1568
 Furtak L. J., Shuntov M., Atek H., Zitrin A., Richard J., Lehnert M. D., Chevallard J., 2023, *MNRAS*, 519, 3064
 Giavalisco M., et al., 2004, *ApJ*, 600, L93
 Giménez-Arteaga C., et al., 2023, *ApJ*, 948, 126
 Grazian A., et al., 2015, *A&A*, 575, A96
 Guo Y., et al., 2016, *ApJ*, 833, 37
 Hainline K. N., et al., 2024, *ApJ*, 964, 71
 Harikane Y., et al., 2023, *ApJS*, 265, 5
 Ishigaki M., Kawamata R., Ouchi M., Oguri M., Shimasaku K., Ono Y., 2015, *ApJ*, 799, 12
 Juodžbalis I., et al., 2023, *MNRAS*, 525, 1353
 Kroupa P., 2002, *Science*, 295, 82
 Laporte N., Meyer R. A., Ellis R. S., Robertson B. E., Chisholm J., Robertson Borsani G. W., 2021, *MNRAS*, 505, 3336
 Larson R. L., et al., 2023, *ApJ*, 958, 141
 Leung G. C. K., et al., 2023, *ApJ*, 954, L46
 Looser T. J., et al., 2025, *A&A*, 697, A88
 Lower S., Narayanan D., Leja J., Johnson B. D., Conroy C., Davé R., 2020, *ApJ*, 904, 33
 Mason C. A., Trenti M., Treu T., 2023, *MNRAS*, 521, 497
 McLeod D. J., McLure R. J., Dunlop J. S., 2016, *MNRAS*, 459, 3812
 Morales A. M., et al., 2024, *ApJ*, 964, L24
 Naidu R. P., et al., 2022, *ApJ*, 940, L14
 Nakajima K., Ouchi M., Isobe Y., Harikane Y., Zhang Y., Ono Y., Umeda H., Oguri M., 2023, *ApJS*, 269, 33
 Noeske K. G., et al., 2007, *ApJ*, 660, L43
 Oesch P. A., et al., 2016, *ApJ*, 819, 129

- Oke J. B., Gunn J. E., 1983, *ApJ*, 266, 713
- Ouchi M., Ono Y., Shibuya T., 2020, *ARA&A*, 58, 617
- Planck Collaboration et al., 2020, *A&A*, 641, A6
- Plat A., Charlot S., Bruzual G., Feltre A., Vidal-García A., Morisset C., Chevallard J., Todt H., 2019, *MNRAS*, 490, 978
- Pontoppidan K. M., et al., 2022, *ApJ*, 936, L14
- Popesso P., et al., 2023, *MNRAS*, 519, 1526
- Rieke M. J., Kelly D., Horner S., 2005, in Heaney J. B., Burriesci L. G., eds, Society of Photo-Optical Instrumentation Engineers (SPIE) Conference Series Vol. 5904, Cryogenic Optical Systems and Instruments XI. pp 1–8, doi:10.1117/12.615554
- Rieke M. J., et al., 2023a, *PASP*, 135, 028001
- Rieke M. J., et al., 2023b, *ApJS*, 269, 16
- Rigby J., et al., 2023, *PASP*, 135, 048001
- Robertson B., et al., 2023, *arXiv e-prints*, p. arXiv:2312.10033
- Salmon B., et al., 2015, *ApJ*, 799, 183
- Salmon B., et al., 2020, *ApJ*, 889, 189
- Sarkar A., Samui S., 2019, *PASP*, 131, 074101
- Schenker M. A., et al., 2013, *ApJ*, 768, 196
- Scoville N., et al., 2007, *ApJS*, 172, 1
- Speagle J. S., Steinhardt C. L., Capak P. L., Silverman J. D., 2014, *ApJS*, 214, 15
- Stark D. P., 2016, *ARA&A*, 54, 761
- Tacchella S., et al., 2023, *MNRAS*, 522, 6236
- Treu T., et al., 2022, *ApJ*, 935, 110
- Windhorst R. A., et al., 2023, *AJ*, 165, 13
- Witten C. E. C., Laporte N., Katz H., 2023, *ApJ*, 944, 61
- Yang L., et al., 2022, *ApJ*, 938, L17

This paper has been typeset from a $\text{\TeX}/\text{\LaTeX}$ file prepared by the author.